Analysis of Spectral Degradation and Error Compensation in 5G NR Digital Polar Transmitters

Christoph Preissl, *Student Member, IEEE*, Peter Preyler, *Student Member, IEEE*, Thomas Mayer, Andreas Springer, *Member, IEEE*, and Mario Huemer, *Senior Member, IEEE*

Abstract—**Cellular standards evolve to support increasingly higher bandwidths which results in strict in- and out-of-band requirements such as lower error vector magnitude (EVM) and/or adjacent channel leakage ratio (ACLR). Digital polar transmitters, which are showing the best performance in terms of power consumption, are challenged to fulfill these requirements. This work will show that even in case of ideal analog components and infinite digital resources, there are principle limitations in terms of out-of-band noise for digital polar transmitters. A typical polar modulation will be compared to a theoretical signal with continuous amplitude modulation. The analysis of the resulting error signal suggests a decomposition into two components which can be partially compensated in the amplitude and phase modulation paths. Based on that decomposition a compensation algorithm has been developed and evaluated with a 400 MHz 5G New Radio (NR) signal for Band n257 on Frequency Range 2 with carrier frequency of 26.5 GHz. The compensation results in an out-of-band noise reduction of 44 dB close to the carrier frequency. Furthermore, EVM improvements for NR signals are demonstrated.**

Index Terms—**Digital-to-phase converter, DPC, digital-to-time converter, DTC, digital polar transmitter, phase modulation, ACLR, EVM, PLL.**

I. INTRODUCTION

THE complex modulation schemes and wide bandwidths defined in the latest Release 15 of the 3rd Generation Partnership Project (3GPP) are becoming a big challenge for modern cellular communication devices [1]. For cellular radio frequency (RF) transmitters it is expected that they are capable of transmitting modulated carriers for every radio access technology (RAT) with one common hardware. This
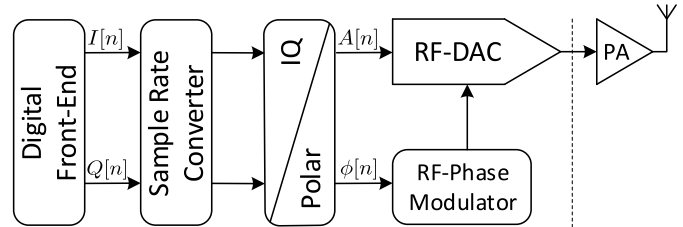
Fig. 1.   Generic block diagram of a digital polar transmitter.

combination of reconfigurability and linearity requirements is best met with digital transmitter architectures. Those architectures achieve better results in terms of power consumption, voltage and temperature variations or power added efficiency (PAE), compared to mostly analog architectures [2]. In the last years different RF transmitter architectures have been published like all-digital-quadrature (IQ) [2]–[7], digital-polar-based [8], [9], multiphase [10], [11], outphasing [12]–[16] or hybrid IQ-polar architectures [17]. The application of digital switching for millimeter waves (mmWave) frequencies is challenging and implementations are not yet shown. Still, it is worth investigating such a structure given that switching speed of transistors still increases over process nodes.

In terms of power consumption the digital-polar-based architecture is the most promising one and will form the basis of this investigation. For example, the polar architecture has a power efficiency gain up to $3\,\mathrm{dB}$ compared to the quadrature signal summation in an IQ architecture [18]. A simplified block diagram of a digital polar transmitter is presented in Fig. 1. In the first step, the $I[n]$ and $Q[n]$ components of the digital baseband signal generated by the digital front-end (DFE) are upsampled in the sample rate converter. Afterwards, the upsampled baseband signals are converted to amplitude and phase components. The phase modulation signal $\phi[n]$ is fed into an RF-phase modulator which is generating a phase modulated square-wave carrier where the positions of rising and falling edges in every RF cycle are controlled. The RF-phase modulator is usually realized by a phase-locked loop (PLL) [19] or via the usage of digital-to-time converters (DTCs) [20]–[24]. In the last step the amplitude signal is applied together with the phase modulated square-wave carrier to a radio frequency digital-to-analog converter (RF-DAC) [25], [26] generating the RF output signal at the desired carrier frequency f_c.

There are two main effects that are responsible for the out-of-band noise in digital polar transmitters and both have an increased impact with higher bandwidths. First, the phase and amplitude components occupy much wider bandwidths than the complex baseband signal itself, because of the nonlinear transformation from cartesian to polar components [27]–[29]. Second, from a signal processing point of view the RF-DAC applies a zero-order-hold (ZOH) operation on the amplitude signal. In the best case scenario, the amplitude signal is sampled on both, rising and falling clock edges and consequently has spectral replicas on even multiples of f_c. On the one hand those spectral replicas are not being entirely attenuated because of the ZOH operation. On the other hand the phase modulated square-wave carrier has its harmonics on odd multiples of f_c. Thus, every spectral replica is folded back to the carrier frequency. The origin of this imperfection can also be reduced to the operation of the mixer in a digital-like manner, even if the input signals are originally created by analog circuitry, which will be more precisely explained in Section III. The impact of this problem will be discussed and a cancellation technique for compensating the spectral degradation close to the carrier frequency is proposed.

Several studies on the spectral degradation of a polar transmitter have already been published. Apart from investigations that focus on limitations like amplitude modulation (AM) and phase modulation (PM) mismatch [30], nonlinearities [20] or circuit noise, there are similar papers investigating principal limitations for polar-like systems. In [13] and [14] an outphasing transmitter is described and limitations and corrections are proposed regarding both phase components. The main novelty of this work is the focus on up-converting the amplitude modulation signal by a phase modulated square-wave carrier and the proposed correction which takes into account not only the phase information but also the amplitude. The tri-phasing apparatus described by [31] is analyzed similarly to the outphasing circuit [13], [14]. The additional multiplication of the amplitude modulation signal with a phase modulated carrier introduces similar imperfections as described in this work. However, the investigation was not necessary in [31] as the total noise contribution of this minor addition to an outphasing system is not significant.

This paper begins by explaining the principle limitations of digital polar transmitters and the challenges of finding the optimal choice for edge locations and amplitude values of the RF output signal in Section II. Section III shows the sources of spectral degradations in digital polar transmitters. Section IV describes an error compensation algorithm and its effects on spectral and EVM improvements. In both Sections III and IV the results are verified by MATLAB simulations for a NR signal with 400 MHz transmission bandwidth on Band n257 with carrier frequency of 26.5 GHz. Finally, conclusions are drawn in Section V.

II. PRINCIPLE LIMITATIONS OF DIGITAL POLAR TRANSMITTERS

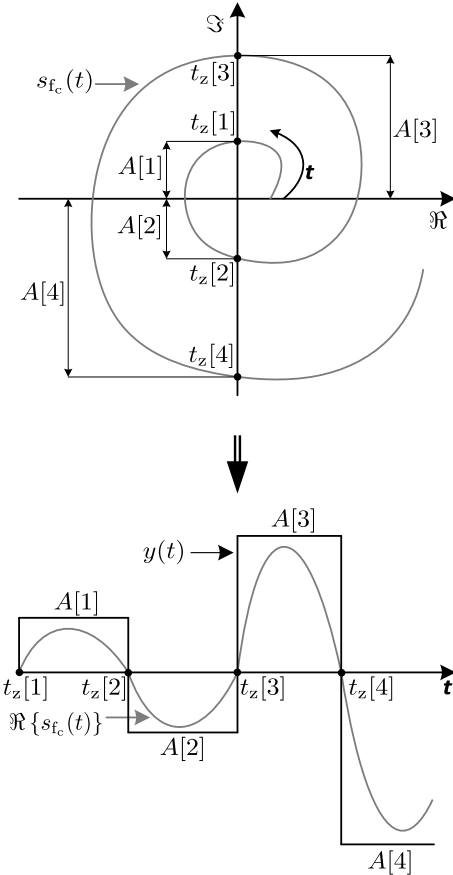In this section an ideal digital polar transmitter is assumed, which means that:

Fig. 2.   Top: complex signal trajectory of $s_{f_c}(t)$. Bottom: derived edge locations $t_z[n]$ and amplitude values $A[n]$ defining the modulated rectangular signal $y(t)$.

1) The digital baseband signals are ideally interpolated via a sinc function.
2) There are no limitations for selecting edge locations and amplitude values for the resulting modulated rectangular signal.
3) There is no mismatch between the AM and the PM processing path.

The complex baseband signal $s(t)$ and the corresponding complex up-converted signal at the carrier frequency f_c are defined as

$$s(t) = I(t) + jQ(t), \tag{1}$$
$$s_{f_c}(t) = s(t)e^{j2\pi f_c t}. \tag{2}$$

The question arises, which modulated rectangular signal $y(t)$ represents the ideal transmitted signal $\Re\left\{s_{f_c}(t)\right\}$ such that the spectral degradation is minimal. The complex signal $s_{f_c}(t)$ does not appear in any practical transmitter architecture but can serve as ideal reference signal for selecting the edge locations $t_z[n]$ and amplitude values $A[n]$ of the modulated rectangular signal. A first and natural choice for $t_z[n]$ would be at the instances in time where the real part of $s_{f_c}(t)$ is passing zero and using the magnitude at this point. The magnitude at this point corresponds to the imaginary part of $s_{f_c}(t)$:

$$\Re\left\{s_{f_c}(t)\right\} = 0 \Rightarrow t_z[n], \tag{3}$$
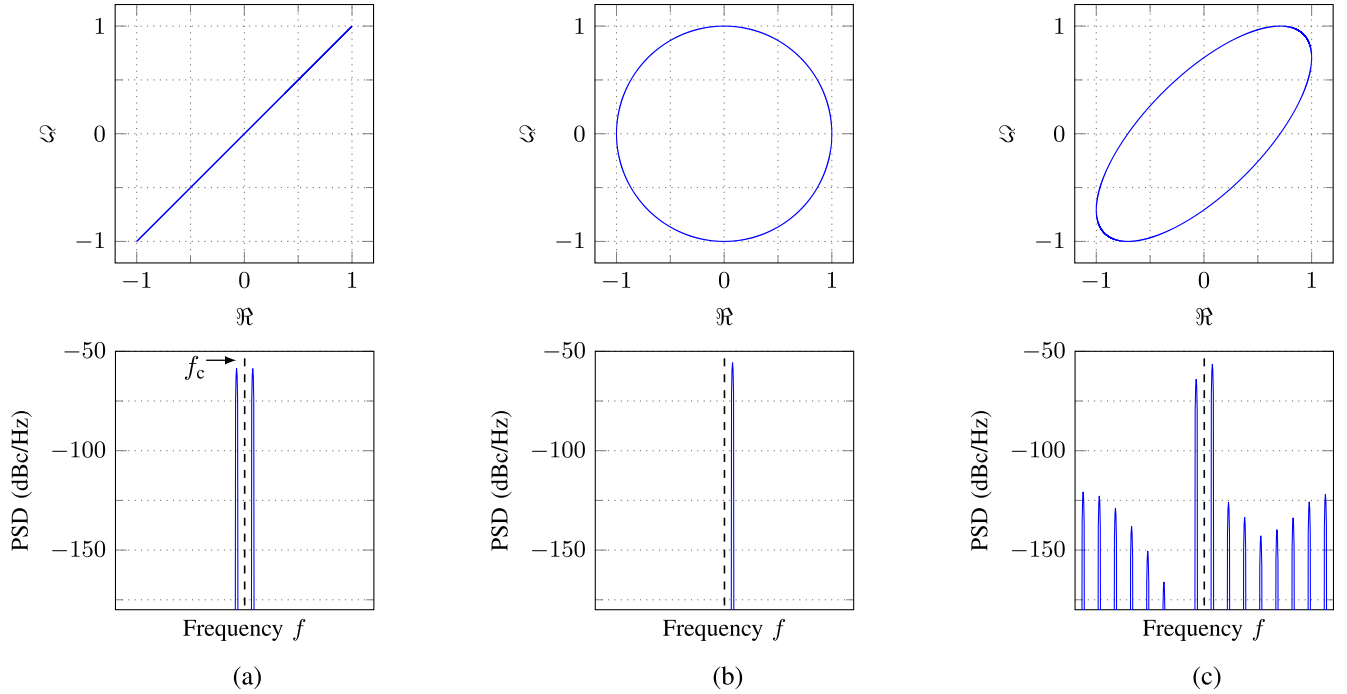$$\Im\left\{s_{f_c}(t_z[n])\right\} \Rightarrow A[n]. \tag{4}$$

Fig. 3. Top row: complex signal trajectory for $s(t) = \cos(2\pi f_{BB}t) + j\cos(2\pi f_{BB}t + \phi)$. Bottom row: resulting PSD of $y(t)$ using $s(t)$ as baseband signal. (a) $\phi = 0$ (amplitude modulation), (b) $\phi = -\frac{\pi}{2}$ (frequency offset), (c) $\phi = -\frac{\pi}{4}$ (amplitude and phase modulation).

By placing edge locations and using amplitude values according to (3) and (4) the resulting modulated rectangular signal $y(t)$, as depicted in Fig. 2, is defined as

$$y(t) = A[n] \quad \text{for } t_z[n] < t \le t_z[n+1]. \tag{5}$$

It will be shown with the help of a very simple baseband signal that it is in general not possible to generate a modulated rectangular signal having no out-of-band noise. To illustrate this, a baseband signal is chosen, whose trajectory is an ellipse in the complex plane

$$s(t) = \cos(2\pi f_{BB}t) + j\cos(2\pi f_{BB}t + \phi), \tag{6}$$

with $-\pi/2 \le \phi \le 0$. Substituting (6) into (2) and calculating its Fourier transform results in

$$\mathcal{F}\{s_{f_c}\}(f) = \frac{1 + j\cos(\phi) - \sin(\phi)}{2}\delta(f - (f_c + f_{BB}))$$
$$+ \frac{1 + j\cos(\phi) + \sin(\phi)}{2}\delta(f - (f_c - f_{BB})). \tag{7}$$

Now, (7) states that the ideal reference signal shows no out-of-band noise and just consists of two Dirac pulses in the frequency domain, each one weighted differently depending on the angle ϕ. The reason to choose this baseband signal is, that it covers three different modulation types. In the first corner case when $\phi = 0$, the signal $s_{f_c}(t)$ is just amplitude modulated. For the second corner case when $\phi = -\frac{\pi}{2}$, a complex exponential frequency offset with f_{BB} results. For all other cases when $-\frac{\pi}{2} < \phi < 0$ the resulting signal $s_{f_c}(t)$ is modulated in amplitude and phase. For the two corner cases it is possible to analytically calculate $t_z[n]$, $A[n]$ and in a next step its Fourier transform. The following calculation shows the

case for $\phi = -\frac{\pi}{2}$: Inserting $\phi = -\frac{\pi}{2}$ into (6) results to

$$s(t) = \cos(2\pi f_{BB}t) + j\cos(2\pi f_{BB}t - \frac{\pi}{2})$$
$$= \cos(2\pi f_{BB}t) + j\sin(2\pi f_{BB}t) = e^{j2\pi f_{BB}t}. \tag{8}$$

By substituting (8) into (2) and using (3), the calculation of the edge locations follows to

$$\Re\left\{e^{j(f_{BB}+f_c)2\pi t}\right\} = 0 \Leftrightarrow \cos((f_{BB} + f_c)2\pi t) = 0 \Leftrightarrow$$
$$2\pi(f_{BB} + f_c)t = n\pi + \frac{\pi}{2} \quad \text{with } n \in \mathbb{Z}. \tag{9}$$

Solving equation (9) leads to

$$t = \frac{2n+1}{4(f_{BB} + f_c)} \Rightarrow t_z[n] = \frac{2n+1}{4(f_{BB} + f_c)}.$$

Given the analytical expression of the edge locations, $y(t)$ can be rewritten as the convolution

$$y(t) = p(t) * \sum_{n=-\infty}^{\infty} \delta(t - t_z[2n]),$$
$$= p(t) * \sum_{n=-\infty}^{\infty} \delta\left(t - \frac{n}{(f_{BB} + f_c)} - \frac{1}{4(f_{BB} + f_c)}\right), \tag{10}$$

with the pulse $p(t)$ defined by

$$p(t) = \begin{cases} 1 & 0 \le t \le T \\ 0 & \text{else}, \end{cases}$$

where the pulse duration T is given as

$$T = t_z[n+1] - t_z[n] = \frac{1}{2(f_{BB} + f_c)}.$$

The Fourier transform of (10) by neglecting the constant phase shift $1/4(f_{\text{BB}} + f_c)$ follows to

$$Y(f) = P(f)(f_{\text{BB}} + f_c) \sum_{k=-\infty}^{\infty} \delta(f - k(f_{\text{BB}} + f_c))$$

$$= e^{-j\pi fT} \frac{\sin(\pi fT)}{\pi f} (f_{\text{BB}} + f_c) \sum_{k=-\infty}^{\infty} \delta(f - k(f_{\text{BB}} + f_c)). \quad (11)$$

(11) shows that the spectrum of the output signal consists of a series of tones which are separated by $f_{\text{BB}} + f_c$

$$Y(k(f_{\text{BB}} + f_c)) = e^{\frac{-j\pi k}{2}} \sin\left(\frac{\pi k}{2}\right) \frac{1}{\pi k}.$$

A similar derivation can be performed for the second corner case with $\phi = 0$. This leads to the same conclusion that the spectrum does not show any out-of-band noise. For the cases where $-\frac{\pi}{2} < \phi < 0$ it is not possible to give a closed form analytical description for $t_z[n]$ and $A[n]$. However, $t_z[n]$ and $A[n]$ can be numerically calculated and as an example the resulting power spectral density (PSD) for the case $\phi = -\frac{\pi}{4}$ is shown in Fig. 3 (c). It can be noticed that in comparison to the cases when $\phi = 0$, depicted in Fig. 3 (a), and $\phi = -\frac{\pi}{2}$, depicted in Fig. 3 (b), unwanted spurs are generated. Note that those spurs arise because the baseband signal defined in (6) is periodic. Baseband signals that are used in communication standards are non-periodic signals. As a consequence, spurs are transformed to a continuous out-of-band noise which is shown in the next section.

III. SOURCES OF SPECTRAL DEGRADATIONS IN DIGITAL POLAR TRANSMITTERS

The previous section demonstrates that a modulated rectangular signal defined in (3) - (5) produces in general out-of-band noise. The question arises if there is a better choice for $t_z[n]$ and $A[n]$. Therefore, the resulting spectral degradation by up-converting the amplitude modulation signal by a phase modulated square-wave carrier is analyzed in more detail. In the first step, the up-conversion of the continuous-time amplitude signal is discussed. It is shown that a noise floor next to the transmitted signal results because of the not ideal recombination of the square-wave harmonics with the amplitude signal. In the second step, an implementable digital polar transmitter is analyzed. It is shown that the up-conversion of the digital amplitude signal generates spectral replicas that are folded back to the carrier frequency. Similar results are shown in [13] and [14] where the root cause of spectral degradation is analyzed for an outphasing transmitter having a discrete-time phase signal.

Assuming the continuous-time phase modulation $\phi(t)$ and amplitude $A(t)$ are given, a mathematical description of the modulated rectangular signal is given by

$$y_{\text{ideal}}^{\text{TX}}(t) = A(t) p_{\text{sq}}(t), \quad (12)$$

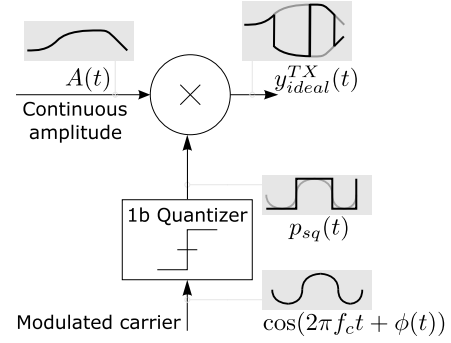with

$$A(t) = |I(t) + jQ(t)|,$$

Fig. 4. The magnitude of the incoming ideal phase modulated carrier $\cos(2\pi f_c t + \phi(t))$ is quantized and results in the ideal phase modulated square-wave carrier $p_{\text{sq}}(t)$. The multiplication of $p_{\text{sq}}(t)$ and $A(t)$ results in the modulated rectangular signal $y_{\text{ideal}}^{\text{TX}}(t)$ having a continuous amplitude.

and the ideal phase modulated square-wave carrier $p_{\text{sq}}(t)$ switching between values 1 and -1 defined as

$$p_{\text{sq}}(t) = \text{sgn}(\cos(2\pi f_c t + \phi(t))),$$
$$\phi(t) = \arg(I(t) + jQ(t)).$$

A block diagram, showing the up-conversion process of the continuous amplitude signal $A(t)$ and as a consequence the generation of $y_{\text{ideal}}^{\text{TX}}(t)$ is presented in Fig. 4.

Now, $p_{\text{sq}}(t)$ can be well approximated by Fourier series theory and (12) results in

$$y_{\text{ideal}}^{\text{TX}}(t) = A(t) \sum_{k=1}^{\infty} a(k) \cos(k(2\pi f_c t + \phi(t))), \quad (13)$$

with the Fourier coefficients $a(k)$ given by

$$a(k) = \frac{4}{k\pi} \sin\left(\frac{k\pi}{2}\right). \quad (14)$$

(13) shows that $A(t)$ is ideally up-converted to the carrier frequency f_c by the fundamental term $a(1) \cos(2\pi f_c t + \phi(t))$. However, the multiplication of $A(t)$ with the remaining harmonic terms $\sum_{k=2}^{\infty} a(k) \cos(k(2\pi f_c t + \phi(t)))$ results in an increased out-of-band contribution and represents a fundamental limit to any digital polar transmitter.

In Fig. 5 the PSD of an NR signal with 400 MHz transmission bandwidth is shown. It will be used as reference signal for the upcoming simulations. Using this reference signal as baseband signal and choosing Band n257 on Frequency Range 2 with a carrier frequency of 26.5 GHz [1] the resulting PSD for $y_{\text{ideal}}^{\text{TX}}(t)$ as well as for $A(t)$ and $p_{\text{sq}}(t)$ are shown in Fig. 6. The optimal combination of $A(t)$ and the fundamental term at f_c, but also a spectral skirt dominated by the first harmonic term can be noticed. The appearing spectral skirt is an inherent problem in every digital polar transmitter. For example in a digital IQ transmitter the fundamental as well as the harmonic terms of the RF output signal are band limited.

The signal defined in (12) cannot be practically realized because it would require a digital polar transmitter which is capable of changing the amplitude continuously in time. Therefore, in every practical output signal the amplitude signal must be held constant from one edge location to the next edge location. Denoting the time instances of zero-crossings of the phase modulated square-wave carrier as in Section II with
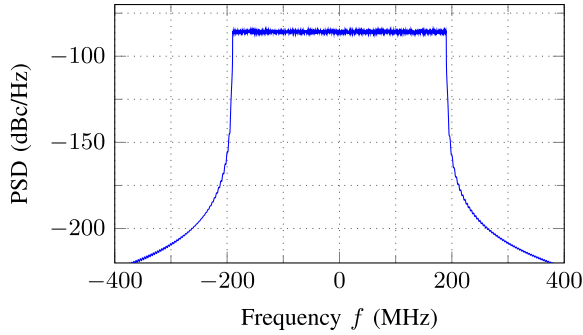
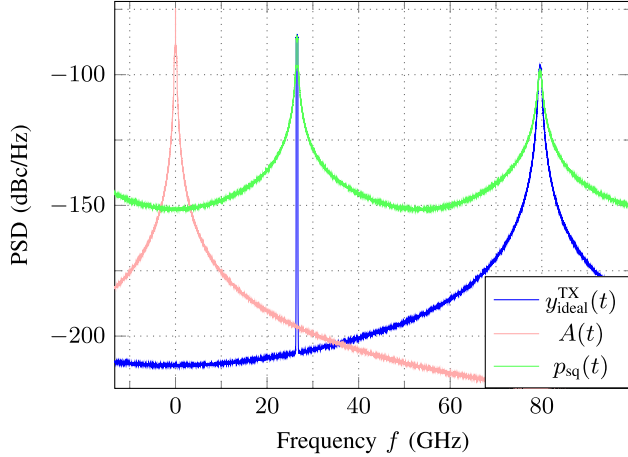Fig. 5. PSD of an NR signal with 400 MHz transmission bandwidth used as reference baseband signal $s(t)$.

Fig. 6. PSDs for the continuous amplitude signal $A(t)$, the phase modulated square-wave carrier $p_{sq}(t)$ and the resulting RF output signal $y_{ideal}^{TX}(t)$ at 26.5 GHz for the 400 MHz baseband signal shown in Fig. 5.

$t_z[n]$, an output signal of the digital polar transmitter can be written as

$$y^{TX}(t) = A_H(t) \, \text{sgn} \left(\cos(2\pi f_c t + \phi(t)) \right), \qquad (15)$$

with

$$A_H(t) = A(t_z[n]) \quad \text{for} \quad t_z[n] < t \le t_z[n+1]. \qquad (16)$$

A block diagram, showing the up-conversion process of the sample and hold amplitude signal $A_H(t)$ and as a consequence the generation of $y^{TX}(t)$, is presented in Fig. 7.

From (16) it can be seen that $A_H(t)$ is sampled on each zero-crossing of the phase modulated square-wave carrier, meaning that its sampling rate is $2f_c$. Consequently, the spectral replicas of $A_H(t)$ are located at frequencies on even multiples of f_c and experience an attenuation due to the sample and hold nature of $A_H(t)$. Since the harmonics of the phase modulated square-wave carrier are located at frequencies on odd multiples of f_c each spectral replica of $A_H(t)$ is folded back to f_c, as depicted in the top of Fig. 8.

To see the spectral degradation of $y^{TX}(t)$ an ideal digital polar transmitter, as defined in Sec. II, is simulated. Using the same baseband signal $s(t)$ from Fig. 5 and for $f_c = 26.5$ GHz a comparison of the PSDs of $y^{TX}(t)$ and $y_{ideal}^{TX}(t)$ is shown in the bottom of Fig. 8. The in-band level and the spectral skirt next to the transmitted signal of $y^{TX}(t)$ are at -85.5 dBc/Hz and -143 dBc/Hz, respectively. The difference between those two levels is now defined as
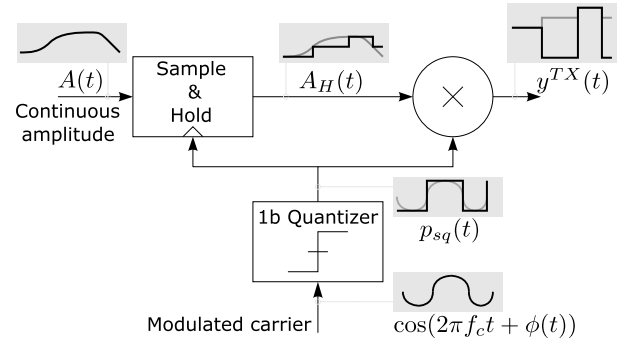

Fig. 7. The magnitudes of the incoming ideal phase modulated carrier $\cos(2\pi f_c t + \phi(t))$ and continuous amplitude signal $A(t)$ are quantized and result in the ideal phase modulated square-wave carrier $p_{sq}(t)$ and sample and hold amplitude $A_H(t)$, respectively. The multiplication of $p_{sq}(t)$ and $A_H(t)$ results in the modulated rectangular signal $y^{TX}(t)$.
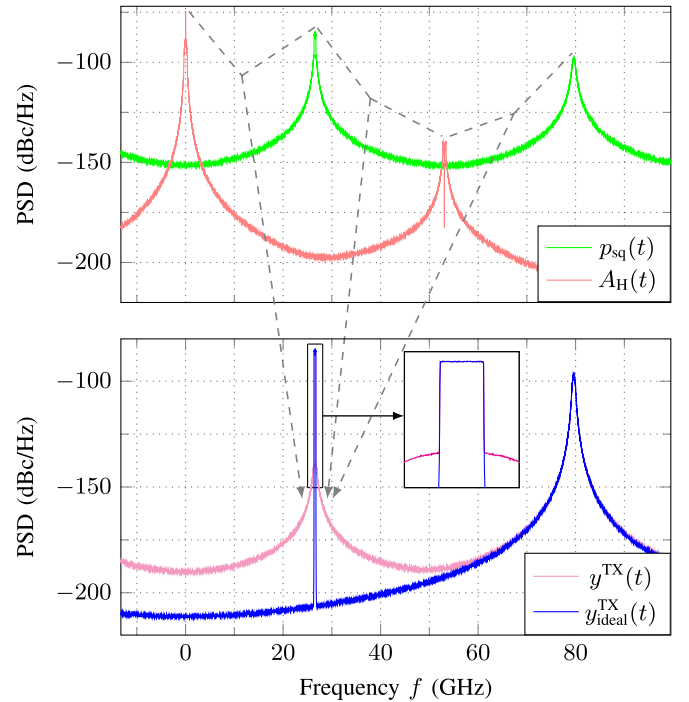

Fig. 8. Top: PSDs of the phase modulated square-wave carrier $p_{sq}(t)$ and the sample and hold amplitude $A_H(t)$. Arrows indicate the mixing products which are folded back to the carrier frequency. Bottom: Spectral comparison between $y^{TX}(t)$ and the fundamental limit $y_{ideal}^{TX}(t)$.

adjacent channel level difference (ACLD). In this context it is noticeable that there is a relationship between the ACLD and the ratio of carrier frequency to transmission bandwidth. Therefore, different carrier frequencies and NR signals from 1 to 400 MHz are simulated for the output signal $y^{TX}(t)$. Afterwards, the mean value of the ACLD is calculated for those simulations with the same ratio of carrier frequency to transmission bandwidth, see Table I. One can see that for a fixed carrier frequency, doubling the transmission bandwidth decreases the ACLD by approximately 6 dB.

IV. ERROR COMPENSATION

Sec. III demonstrated that in any digital polar transmitter a fundamental limitation, in terms of out-of-band noise, is given

TABLE I

ACLD AS FUNCTION OF THE RATIO OF CARRIER
FREQUENCY TO TRANSMISSION BANDWIDTH

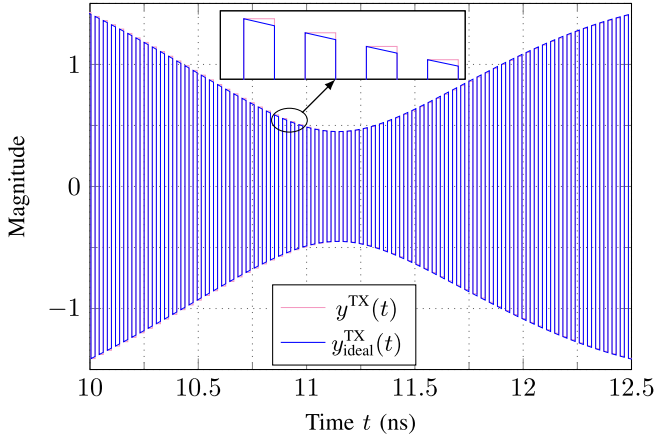| Ratio f_c to bandwidth	ACLD (dB)
256	68.6
128	62.8
64	56.7
32	50.3
16	44.2
8	38.1
4	32.2
2	26.1

Fig. 9. Time segment showing the waveforms of $y^{TX}(t)$ and the fundamental limit $y_{ideal}^{TX}(t)$.

by the ideal signal defined in (12) and a realistic output signal as in (15) shows additional significant spectral degradation. With increased bandwidth this effect becomes even more pronounced.

In this section the obtained results are used to analyze and compensate the error, i.e. the difference between (12) and (15). From a practical perspective it is sufficient to compensate the error at the carrier frequency because it can be assumed that the higher harmonic error components are removed by the RF-DAC matching network. In a digital polar transmitter, there are two possibilities to compensate the error. The first one is to change the amplitude and the other one is to adapt the zero crossings of the modulated rectangular signal. In the following, possible ways and restrictions to compensate for the error are discussed.

A. Compensation With a Rectangular Pulse Train

In Fig. 9 the time domain waveforms of $y^{TX}(t)$ and $y_{ideal}^{TX}(t)$ are shown. The error due to the sample-and-hold nature of $y^{TX}(t)$ is given as

$$e(t) = y_{ideal}^{TX}(t) - y^{TX}(t). \tag{17}$$

Due to the slowly changing amplitude of the signal compared to the carrier frequency the error over each carrier period can be approximated as a piecewise linear function as being depicted in Fig. 10. Additionally, the error shows a shape that can be decomposed into a square wave part $e_s(t)$ and a
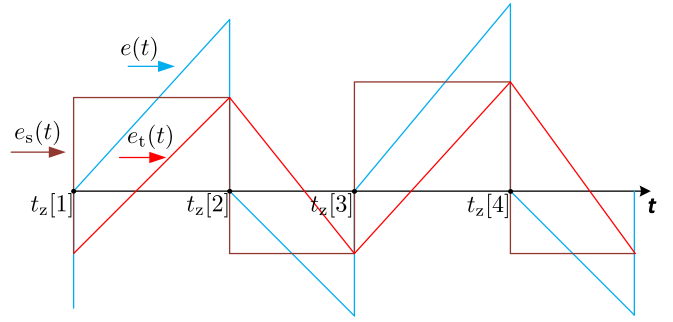

Fig. 10. Piecewise linear behavior of the error signal $e(t)$ over each RF-clock cycle. $e(t)$ can be decomposed into the square wave part $e_s(t)$ and the triangular part $e_t(t)$.

triangular part $e_t(t)$. Since $e_s(t)$ and $y^{TX}(t)$ have the same zero crossings the error compensation for $e_s(t)$ can be accomplished in the amplitude path. The corrected amplitude of $y^{TX}(t)$ that is fully canceling $e_s(t)$ is defined as

$$\tilde{A}_H(t) = A_H(t) + e_s(t). \tag{18}$$

The waveform of the remaining error $e_t(t)$ shows approximately a $\pi/2$ phase offset to $y^{TX}(t)$ and thus cannot be canceled via an amplitude correction. However, as a first step to compensate $e_t(t)$, a pulse train $p_{tr}(t)$ with the same centroids and power as $e_t(t)$ can be created. To realize the same power, the time domain waveforms of $e_t(t)$ and $p_{tr}(t)$ shall have the same area over each half RF clock cycle. Denoting the zero crossings and centroids of $e_t(t)$ as $z_{et}[n]$ and $c[n]$, respectively, the compensation pulse train $p_{tr}(t)$ is shown in Fig. 11. $p_{tr}(t)$ is defined such that the following equation holds

$$\int_{z_{et}[n]}^{z_{et}[n+1]} e_t(t)\,dt = \int_{c[n]-\frac{pw}{2}}^{c[n]+\frac{pw}{2}} p_{tr}(t)\,dt \quad \forall n, \tag{19}$$

where the selected pulse-width pw has to fulfill that

$$pw < \min(c[n+1] - c[n]) \quad \forall n,$$

in order to have no overlaps between the pulses. The pulse train amplitude is automatically adjusted to the selected pulse-width. Please note that the selection of pw has no influence in terms of spectral compensation. In Fig. 12 a spectral comparison of $e_t(t)$ and $p_{tr}(t)$ is given. One can see that at the carrier frequency the PSDs do not match perfectly. However, a constant α can be introduced that is scaling the compensation pulse train $p_{tr}(t)$ such that the spectral level at the carrier frequency is the same as for $e_t(t)$. The total compensation including the scaled compensation pulse train $p_{tr}(t)$ and the corrected amplitude defined in (18) is shown in Fig. 13. One can see that around the carrier frequency the out-of-band noise is decreased by 50 dB compared to $y^{TX}(t)$.

Note that adding the compensation pulse train $p_{tr}(t)$ to $y^{TX}(t)$ results in an effective second carrier with a $\pi/2$ offset to the main carrier $y^{TX}(t)$, similar to the Q component of an IQ-architecture, but with much smaller Q component. To realize the compensation with a digital polar transmitter one would need to change the amplitude values six times on each
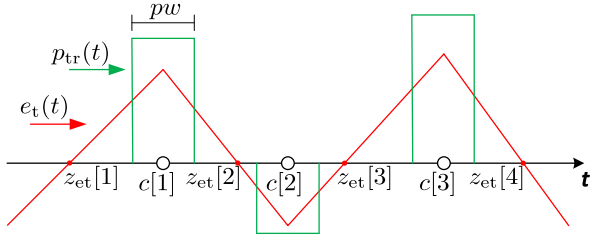
Fig. 11. Compensation pulse train $p_{tr}(t)$ canceling the remaining triangular error $e_t(t)$.
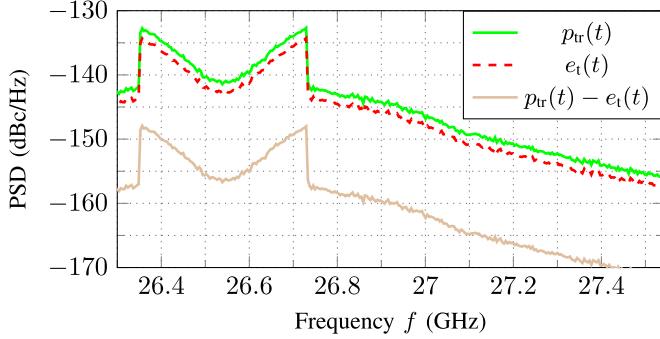

Fig. 12. The difference at carrier frequency between the triangular error $e_t(t)$ and the compensation pulse train $p_{tr}(t)$ by using the same area over each half RF clock cycle shown in the frequency domain as PSD.
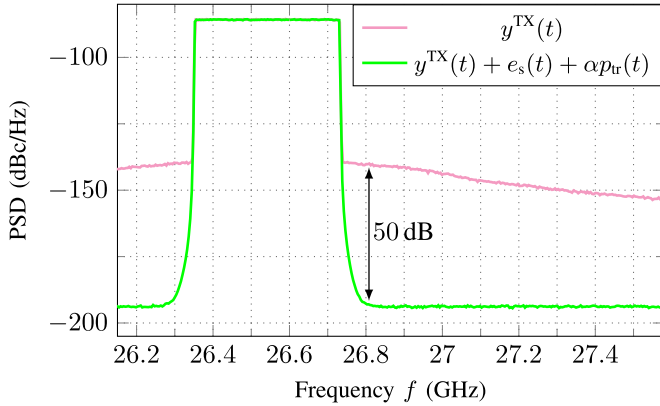

Fig. 13. Adding the square wave part $e_s(t)$ and the scaled compensation pulse train $\alpha p_{tr}(t)$ to the modulated rectangular signal $y^{TX}(t)$ results in a huge spectral improvement around the carrier frequency.

RF clock cycle which is a huge challenge for implementation. Therefore, a different way of adding the pulse train to the main carrier must be considered.

B. Compensation by Shifting the Edge Locations

In the previous subsection it was shown that the error compensation can be accomplished with an amplitude correction and the addition of an appropriate pulse train. Since this pulse train cannot be generated with a single digital polar transmitter a different way to incorporate it into the signal is required. Similar concepts of shifting edge locations in order to decrease the spectral degradation have been presented in [20] and [31]. The main difference of the correction technique in this work
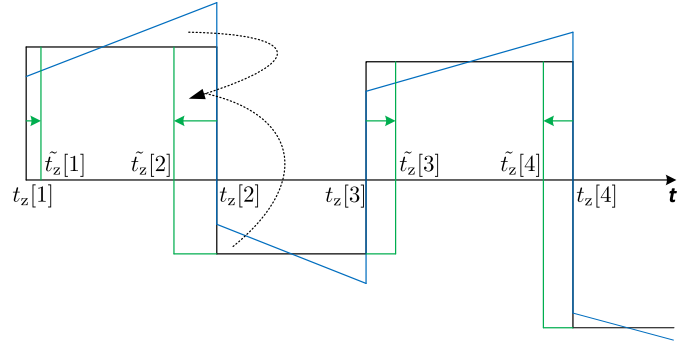

Fig. 14. In order to realize the compensation pulse train $p_{tr}(t)$ with a single digital polar transmitter the edge locations $t_z[n]$ are shifted to $\tilde{t}_z[n]$.

is the combination of the sample-and-hold amplitude signal with a phase modulated square-wave carrier.

From the time-domain comparison in Fig. 11, it can be seen that the centroids of $p_{tr}(t)$ are typically very close to the edge locations of $y^{TX}(t)$. This leads to the idea of an addition of a pulse-train like in the previous subsection, but with the same amplitude as $y^{TX}(t)$ and such that one edge location is identical to the edge location of $y^{TX}(t)$ on each half RF clock cycle. The addition of this adapted pulse-train to $y^{TX}(t)$ results in an effective shift of the edge locations from $t_z[n]$ to $\tilde{t}_z[n]$, as it is depicted in Fig. 14. Shifting the edge locations results in a small phase error compared to the addition of the ideal compensation pulse train $p_{tr}(t)$, which limits the achievable improvement. However, the signal that will be added to $y^{TX}(t)$ still shows a significant spectral improvement while presenting a modulation signal that can be realized with a digital polar transmitter. The corrected rectangular signal $y_{corr}^{TX}(t)$, that includes both the amplitude correction and the changed edge locations to incorporate the pulse-train is now defined as

$$y_{corr}^{TX}(t) = \tilde{A}_H(t) \text{ for } \tilde{t}_z[n] < t \le \tilde{t}_z[n+1], \qquad (20)$$

with the corrected amplitude defined in (18) and the corrected edge locations

$$\tilde{t}_z[n] = t_z[n] + \frac{\alpha \int_{z_{et}[n]}^{z_{et}[n+1]} \left(y_{ideal}^{TX}(t) - y^{TX}(t) \right) dt}{\tilde{A}_H(t_z[n-1]) + \tilde{A}_H(t_z[n])}. \qquad (21)$$

The following points should be noted for the calculation of $y_{corr}^{TX}(t)$:

1) The amplitude correction in (18) is ideal, meaning that it cancels the error square wave part $e_s(t)$ completely. For any practical implementation a reasonable approximation for $\tilde{A}_H(t)$ is to sample the amplitude signal half way between the edge locations, i.e.

$$\hat{A}_H(t) = \frac{A(\tilde{t}_z[n]) + A(\tilde{t}_z[n+1])}{2} \quad \text{for } \tilde{t}_z[n] < t \le \tilde{t}_z[n+1].$$

2) Since the zero crossings $z_{et}[n]$ of $e_t(t)$ are approximately located half way between the two edge locations, the boundaries for the area calculation in (21) can be approximated by $(\tilde{t}_z[n-1]+\tilde{t}_z[n])/2$ and $(\tilde{t}_z[n]+\tilde{t}_z[n+1])/2$. In the calculation of (21) the constant α is assumed to be

TABLE II

COMPARISON OF THE ACLD AS A FUNCTION OF THE RATIO OF CARRIER FREQUENCY TO TRANSMISSION BANDWIDTH FOR $y^{\mathrm{TX}}(t)$ AND $y^{\mathrm{TX}}_{\mathrm{CORR}}(t)$. THE RIGHT COLUMN MARKED IN GREEN DEMONSTRATES THE SPECTRAL IMPROVEMENT WHEN BOTH AMPLITUDE AND EDGE LOCATION CORRECTIONS ARE INCLUDED

Ratio f_{c} to bandwidth	ACLD $y^{\mathrm{TX}}(t)$ (dB)	ACLD $y^{\mathrm{TX}}_{\mathrm{corr}}(t)$ (dB)	Out-of-band noise improvement (dB)
256	68.6	128.7	60.1
128	62.8	115.7	52.9
64	56.7	101.9	45.2
32	50.3	89.2	38.9
16	44.2	75.1	30.9
8	38.1	60.9	22.8
4	32.2	47.6	15.4
2	26.1	33.3	7.2
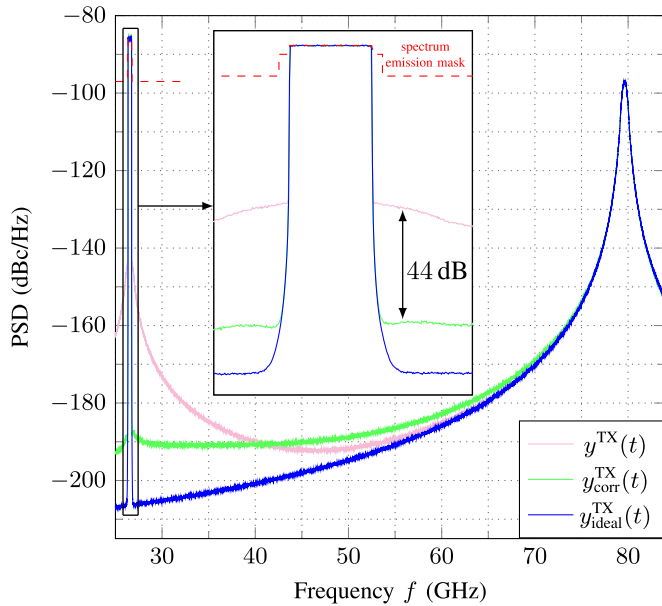
Fig. 15. Spectral comparison between $y^{\mathrm{TX}}(t)$, $y^{\mathrm{TX}}_{\mathrm{corr}}(t)$ and $y^{\mathrm{TX}}_{\mathrm{ideal}}(t)$ using the 400 MHz reference baseband signal at 26.5 GHz. $y^{\mathrm{TX}}_{\mathrm{corr}}(t)$, that is having the corrected amplitude and edge locations, decreases the out-of-band noise close to the carrier frequency by 44 dB. The huge gap to the spectrum emission mask comes from the fact that an ideal digital polar transmitter is assumed.

Fig. 16. PSDs for $y^{\mathrm{TX}}_{\mathrm{corr}}(t)$ using different numbers of bits m for the amplitude quantization. A minimum of 8 bits is necessary to decrease the out-of-band noise compared to $y^{\mathrm{TX}}(t)$. For $m \geq 15$ the theoretical limit is practically achieved.

ideal in the sense that the fundamental of the correction pulse train matches perfectly the fundamental of $e_{\mathrm{t}}(t)$.

In Fig. 15 a spectral comparison between $y^{\mathrm{TX}}(t)$, the corrected $y^{\mathrm{TX}}_{\mathrm{corr}}(t)$ and the fundamental limit $y^{\mathrm{TX}}_{\mathrm{ideal}}(t)$ is shown. Once again, the same configuration like in the previous section is used, i.e. the baseband signal from Fig. 5 and Band n257 with $f_{\mathrm{c}} = 26.5$ GHz. $y^{\mathrm{TX}}_{\mathrm{corr}}(t)$ decreases the out-of-band noise close to the carrier frequency by 44 dB compared to $y^{\mathrm{TX}}(t)$. The level of the out-of-band spectrum is significantly below the mask given by the 3GPP for the used carrier frequency and bandwidth combination [1]. Consequently, there is much room for additional out-of-band degradations like nonideal components [20] or AM and PM mismatch [30]. However, the investigated effect scales with bandwidth to carrier frequency and poses a fundamental limitation that needs to be considered in scenarios where the ratio becomes smaller. It should be noted that for very small ratios the level of out of band noise is dominated by the noise of the nearby harmonics.
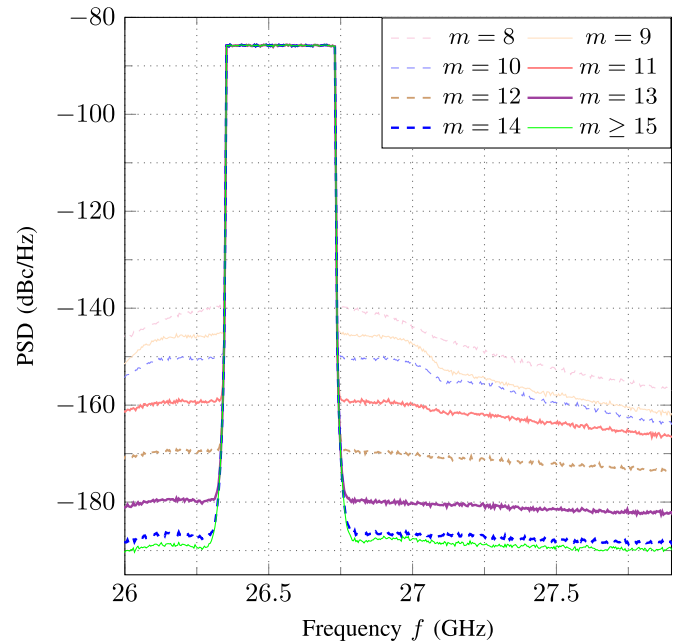
Different carrier frequencies and bandwidth combinations are simulated for $y^{\mathrm{TX}}_{\mathrm{corr}}(t)$. The results are summarized in Table II. In its third column the mean value of the ACLD of $y^{\mathrm{TX}}_{\mathrm{corr}}(t)$ is calculated for those simulations with the same ratio of carrier frequency to transmission bandwidth. By doubling this ratio, the ACLD of $y^{\mathrm{TX}}_{\mathrm{corr}}(t)$ increases between 13 dB and 14 dB. Furthermore, the green column illustrates the out-of-band noise improvement around the carrier frequency when the amplitude and edge location corrections are included.

Fig. 15 presents results of a simulation having ideal components in the whole transmitter chain. In the following, different oversampling rates and quantization resolutions for the proposed compensation method are investigated with respect to spectral improvements. First, for the calculation in (21), the approximations $\hat{A}_{\mathrm{H}}(t)$, $(\tilde{t}_{\mathrm{z}}[n-1] + \tilde{t}_{\mathrm{z}}[n])/2$ and $(\tilde{t}_{\mathrm{z}}[n] + \tilde{t}_{\mathrm{z}}[n+1])/2$ are used instead of $\tilde{A}_{\mathrm{H}}(t)$, $z_{\mathrm{et}}[n]$ and $z_{\mathrm{et}}[n+1]$, respectively. Second, a limited number of bits for representing the amplitude values in fixed point representation
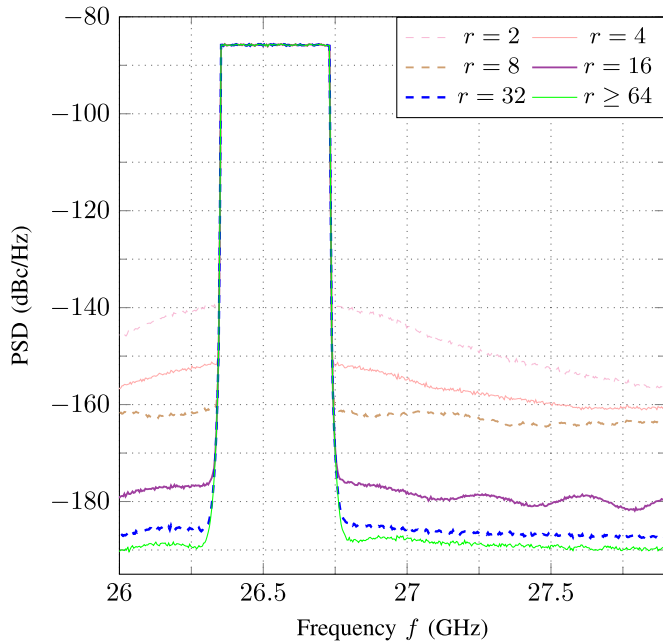
Fig. 17. PSDs for $y_{corr}^{TX}(t)$ having 15 bits for the amplitude quantization and using different oversampling rates r. The oversampling rate r relates to the sampling frequency of $r \cdot f_c$ Hz and r integration points are used for the numerical integration in (21). A minimum of $r = 2$ is necessary to decrease the out-of-band noise compared to $y^{TX}(t)$. For oversampling rates $r \geq 64$ the theoretical limit is practically achieved.
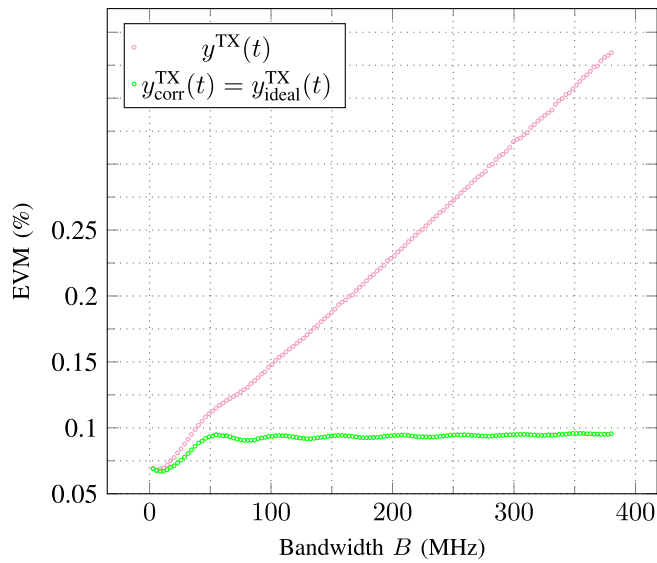

Fig. 18. EVM simulation result for increasing number of RBs of an NR 400 signal.

is assumed. Fig. 16 shows the impact of having different numbers of bits m available for calculating $y_{corr}^{TX}(t)$. The theoretical limit is practically achieved with 15 bits quantization, the increase of the out-of-band noise with decreasing number of bits is highlighted in the figure. Furthermore, in (21) the occurring integral must be numerically integrated for each $\tilde{t}_z[n]$. In Fig. 17 different power-of-two oversampling rates r from 2 to 64 are simulated. An oversampling rate of r means that the actual sampling frequency is $r \cdot f_c$ Hz,

and the numerical integration is done via the left Riemann sum having r integration points. In can be noticed that an oversampling rate of $r = 2$ is necessary, in order to decrease the out-of-band noise compared to $y^{TX}(t)$ and the limit of spectral improvements is practically reached with $r \geq 64$. Clearly, in a practical implementation the oversampling rates and the number of bits for the quantization resolution depend on the available noise budget.

Finally, Fig. 18 shows simulation results for an NR 400 signal where the number of RBs is successively increased from 1 to 264. For each simulation the EVM for $y^{TX}(t)$, $y_{corr}^{TX}(t)$ and $y_{ideal}^{TX}(t)$ is calculated with 15 bits and $r = 64$ for the quantization resolution and oversampling rate, respectively. It can be seen that the error for $y^{TX}(t)$ increases with bandwidth. The discrepancy between $y_{corr}^{TX}(t)$ and $y_{ideal}^{TX}(t)$ is not noticeable and the error for both signals remains constant. Compared to the 3GPP EVM requirement of 8% for 64QAM [1], the level of $y_{corr}^{TX}(t)$ is very small. However, this result contributes to an overall budget for EVM and the requirements for future standards are getting more demanding.

V. CONCLUSION

In this work, fundamental limitations in terms of out-of-band noise in digital polar transmitters have been analyzed. Especially the inherent problem of folded spectral replicas of the ZOH amplitude signal causes a severe spectral degradation close to the carrier frequency. This effect becomes even more critical with wider bandwidth. A theoretical signal has been defined that illustrates the principal spectral limitations for digital polar transmitters. Polar signals generated by classic sample and hold operation show significantly more out-of-band noise compared to this theoretical signal. By time domain comparison a compensation for the sample and hold signal can be constructed, which drastically decreases the out-of-band noise. It turns out that the resulting error signal shows a piecewise linear behavior that can be decomposed into a square wave and triangular part. The square wave part can be completely compensated via adapting the amplitude signal. The triangular part can be partially compensated by a pulse train which can be approximately added via correcting the edge locations of the modulated rectangular signal. The significant spectral improvement around the carrier frequency has been verified by MATLAB simulation results with NR signals.

REFERENCES

[1] *NR; User Equipment (UE) Radio Transmission and Reception; Part 2: Range 2 Standalone, Version 16.1.0*, document 38.101-2, 3rd Generation Partnership Project (3GPP), 2019.
[2] R. B. Staszewski, "Digitally intensive wireless transceivers," *IEEE Des. Test Comput.*, vol. 29, no. 6, pp. 7–18, Dec. 2012.
[3] H. Wang *et al.*, "A highly-efficient multi-band multi-mode all-digital quadrature transmitter," *IEEE Trans. Circuits Syst. I, Reg. Papers*, vol. 61, no. 5, pp. 1321–1330, May 2014.

[4] D. Kim, H. Jin, S. Jin, and B. Kim, "Highly efficient and wideband digital quadrature transmitter," in *IEEE MTT-S Int. Microw. Symp. Dig.*, Jun. 2013, pp. 1–3.

[5] M. S. Alavi, R. B. Staszewski, L. C. N. de Vreede, and J. R. Long, "A wideband 2×13-bit all-digital I/Q RF-DAC," *IEEE Trans. Microw. Theory Techn.*, vol. 62, no. 4, pp. 732–752, Apr. 2014.

[6] M. Mehrpoo, M. Hashemi, Y. Shen, L. C. N. de Vreede, and M. S. Alavi, "A wideband linear I/Q-interleaving DDRM," *IEEE J. Solid-State Circuits*, vol. 53, no. 5, pp. 1361–1373, May 2018.

[7] J. Markovic, D. Hamidovic, C. Mayer, J. Zaleski, M. Huemer, and A. Springer, "An IQ image cancellation method for digital-intensive transmitters," in *Proc. IEEE Int. Symp. Circuits Syst. (ISCAS)*, May 2019, pp. 1–5.

[8] Z. Boos *et al.*, "A fully digital multimode polar transmitter employing 17b RF DAC in 3G mode," in *IEEE Int. Solid-State Circuits Conf. (ISSCC) Dig. Tech. Papers*, Feb. 2011, pp. 376–378.

[9] M. Fulde *et al.*, "13.2 A digital multimode polar transmitter supporting 40MHz LTE carrier aggregation in 28nm CMOS," in *IEEE Int. Solid-State Circuits Conf. (ISSCC) Dig. Tech. Papers*, Feb. 2017, pp. 218–219.

[10] W. Yuan and J. S. Walling, "A multiphase switched capacitor power amplifier," *IEEE J. Solid-State Circuits*, vol. 52, no. 5, pp. 1320–1330, May 2017.

[11] D. Hamidovic, J. Markovic, P. Preyler, C. Mayer, M. Huemer, and A. Springer, "A comparison of all-digital transmitter architectures for cellular handsets," in *Proc. Austrochip Workshop Microelectron. (Austrochip)*, Oct. 2019, pp. 14–20.

[12] A. Ravi *et al.*, "A 2.4-GHz 2–40-MHz channel WLAN digital outphasing transmitter utilizing a delay-based wideband phase modulator in 32-nm CMOS," *IEEE J. Solid-State Circuits*, vol. 47, no. 12, pp. 3184–3196, Dec. 2012.

[13] D. Seebacher, P. Singerl, C. Schuberth, F. Dielacher, P. Reynaert, and W. Bosch, "Reduction of aliasing effects of RF PWM modulated signals by cross point estimation," *IEEE Trans. Circuits Syst. I, Reg. Papers*, vol. 61, no. 11, pp. 3184–3192, Nov. 2014.

[14] J. Lemberg *et al.*, "Digital interpolating phase modulator for wideband outphasing transmitters," *IEEE Trans. Circuits Syst. I, Reg. Papers*, vol. 63, no. 5, pp. 705–715, May 2016.

[15] M. Kosunen *et al.*, "13.5 a 0.35-to-2.6GHz multilevel outphasing transmitter with a digital interpolating phase modulator enabling up to 400MHz instantaneous bandwidth," in *Proc. IEEE Int. Solid-State Circuits Conf. (ISSCC)*, Feb. 2017, pp. 224–225.

[16] Z. Hu, L. C. N. de Vreede, M. S. Alavi, D. A. Calvillo-Cortes, R. B. Staszewski, and S. He, "A 5.9 GHz RFDAC-based outphasing power amplifier in 40-nm CMOS with 49.2% efficiency and 22.2 dBm power," in *Proc. IEEE Radio Freq. Integr. Circuits Symp. (RFIC)*, May 2016, pp. 206–209.

[17] T. Buckel *et al.*, "A novel digital-intensive hybrid polar-I/Q RF transmitter architecture," *IEEE Trans. Circuits Syst. I, Reg. Papers*, vol. 65, no. 12, pp. 4390–4403, Dec. 2018.

[18] N. Ginzberg and E. Cohen, "Switched-capacitor RF power amplifiers: A review of efficiency and linearity considerations," in *Proc. IEEE Int. Conf. Sci. Electr. Eng. Isr. (ICSEE)*, Dec. 2018, pp. 1–5.

[19] T. Buckel *et al.*, "A highly reconfigurable RF-DPLL phase modulator for polar transmitters in cellular RFICs," *IEEE Trans. Microw. Theory Techn.*, vol. 66, no. 6, pp. 2618–2627, Jun. 2018.

[20] P. Madoglio *et al.*, "13.6 A 2.4 GHz WLAN digital polar transmitter with synthesized digital-to-time converter in 14 nm trigate/FinFET technology for IoT and wearable applications," in *IEEE Int. Solid-State Circuits Conf. (ISSCC) Dig. Tech. Papers*, Feb. 2017, pp. 226–227.

[21] S. A. Talwalkar, "Quantization error spectra structure of a DTC synthesizer via the DFT axis scaling property," *IEEE Trans. Circuits Syst. I, Reg. Papers*, vol. 59, no. 6, pp. 1242–1250, Jun. 2012.

[22] S. Sievert *et al.*, "A 2 GHz 244 fs-resolution 1.2 ps-peak-INL edge interpolator-based digital-to-time converter in 28 nm CMOS," *IEEE J. Solid-State Circuits*, vol. 51, no. 12, pp. 2992–3004, Dec. 2016.

[23] P. Preyler, C. Preissl, S. Tertinek, T. Buckel, and A. Springer, "LO generation with a phase interpolator digital-to-time converter," *IEEE Trans. Microw. Theory Techn.*, vol. 65, no. 11, pp. 4669–4676, Sep. 2017.

[24] Y. Palaskas *et al.*, "A cellular multiband DTC-based digital polar transmitter with −153 dBc/Hz noise in 14-nm FinFET," *IEEE Solid-State Circuits Lett.*, vol. 2, no. 9, pp. 179–182, Sep. 2019.

[25] S. Luschas, R. Schreier, and H.-S. Lee, "Radio frequency digital-to-analog converter," *IEEE J. Solid-State Circuits*, vol. 39, no. 9, pp. 1462–1467, Sep. 2004.

[26] S.-M. Yoo, J. S. Walling, E. C. Woo, B. Jann, and D. J. Allstot, "A switched-capacitor RF power amplifier," *IEEE J. Solid-State Circuits*, vol. 46, no. 12, pp. 2977–2987, Dec. 2011.

[27] G. Strasser, B. Lindner, L. Maurer, G. Hueber, and A. Springer, "On the spectral regrowth in polar transmitters," in *IEEE MTT-S Int. Microw. Symp. Dig.*, Jun. 2006, pp. 781–784.

[28] B. Lindner, G. Strasser, L. Maurer, Z. Boos, and R. Hagelauer, "Bandlimiting polar signals with special W-CDMA constellations," in *Proc. Eur. Conf. Wireless Technol.*, Oct. 2007, pp. 32–35.

[29] I. L. Syllaios, P. T. Balsara, and R. B. Staszewski, "Recombination of envelope and phase paths in wideband polar transmitters," *IEEE Trans. Circuits Syst. I, Reg. Papers*, vol. 57, no. 8, pp. 1891–1904, Aug. 2010.

[30] K. Waheed, R. B. Staszewski, and S. Rezeq, "Curse of digital polar transmission: Precise delay alignment in amplitude and phase modulation paths," in *Proc. IEEE Int. Symp. Circuits Syst.*, May 2008, pp. 3142–3145.

[31] J. Lemberg *et al.*, "A 1.5–1.9-GHz all-digital tri-phasing transmitter with an integrated multilevel class-D power amplifier achieving 100-MHz RF bandwidth," *IEEE J. Solid-State Circuits*, vol. 54, no. 6, pp. 1517–1527, Jun. 2019.

Christoph Preissl (Student Member, IEEE) received the bachelor's and master's degrees in technical and industrial mathematics from Johannes Kepler University, Linz, Austria, in 2010 and 2013, respectively. In 2014, he joined Danube Mobile Communications Engineering GmbH & Company KG (majority owned by Intel Austria GmbH), Linz, as a Ph.D. Student. Since 2018, he has been a part of the Christian Doppler Laboratory for Digitally Assisted RF Transceivers for Future Mobile Communications, Johannes Kepler University. His current research interests are in the area of digital-intensive RF transceiver architectures.

Peter Preyler (Student Member, IEEE) received the M.Sc. degree in mechatronics from Johannes Kepler University, Linz, Austria, in 2016, where he is currently pursuing the Ph.D. degree. In 2012, he joined Danube Mobile Communications Engineering GmbH & Company KG (majority owned by Intel Austria GmbH), Linz. Since 2018, he has been a part of the Christian Doppler Laboratory for Digitally Assisted RF Transceivers for Future Mobile Communications, University of Linz, Austria. His current research interests are in the area of digital-intensive transceiver architectures.

Thomas Mayer received the Dipl.Ing. and Ph.D. degrees in electrical engineering from Johannes Kepler University, Linz, Austria, in 2002 and 2006, respectively. He joined DICE GmbH & Company KG, a subsidiary of Infineon Technologies in 2002. Since 2011, he has been with Danube Mobile Communications Engineering GmbH & Company KG (majority owned by Intel Austria GmbH), Linz, Austria, where he is currently a Principal Engineer involved in RF LO generation and modulation, phase locked loops, and transmit architectures for cellular transceivers.

Andreas Springer (Member, IEEE) received the Dr.Techn. (Ph.D.) degree and the Univ.-Doz. (Habilitation) degree from Johannes Kepler University (JKU), Linz, Austria, in 1996 and 2001, respectively.

From 1991 to 1996, he was with the Microelectronics Institute, JKU. In 1997, he joined the Institute for Communications and Information Engineering, JKU, where he became a Full Professor in 2005. Since July 2002, he has been the Head of the Institute for Communications Engineering and RF-Systems (formerly Institute for Communications and Information Engineering), JKU. In the Austrian K2 Center for Symbiotic Mechatronics, he serves as a Research Area Coordinator. Since 2017, he has been a Co-Leader of the Christian Doppler Lab for Digitally Assisted RF Transceivers for Future Mobile Communications. His current research interests are focused on wireless communication systems, single and multi carrier communications, architectures and algorithms for multiband/multimode transceivers, wireless sensor networks, and recently millimeter wave communications. In these fields, he has published more than 250 articles in journals and at international conferences, one book, and two book chapters. He is a member of the IEEE Microwave Theory and Techniques, the Communications, and the Vehicular Technology societies, OVE, and VDI. In 2006, he was a co-recipient of the Science Price of the German Aerospace Center (DLR). From 2002 to 2012, he served as a Chair for the IEEE Austrian Joint COM/MTT Chapter. He was a member of the Editorial Board of the *International Journal of Electronics and Communications* (AEÜ) from 2012 to 2019. He serves as a reviewer for a number of international journals and conferences.

Mario Huemer (Senior Member, IEEE) received the Dipl.-Ing. and Dr.techn. degrees from Johannes Kepler University (JKU), Linz, Austria, in 1996 and 1999, respectively.

After holding positions in industry and academia, he was an Associate Professor at the University of Erlangen-Nuremberg, Germany, from 2004 to 2007, and a Full Professor at Klagenfurt University, Austria, from 2007 to 2013. From 2012 to 2013, he served as the Dean of the Faculty of Technical Sciences. In September 2013, he moved back to Linz, Austria, where he is now heading the Institute of Signal Processing, JKU as a Full Professor. Since 2017, he has been the Co-Head of the "Christian Doppler Laboratory for Digitally Assisted RF Transceivers for Future Mobile Communications." His research focuses on statistical and adaptive signal processing, signal processing architectures and implementations, as well as mixed signal processing with applications in information and communications engineering, radio frequency and baseband integrated circuits, and sensor and biomedical signal processing. Within these fields he has published more than 260 scientific papers.

Dr. Huemer is member of the IEEE Signal Processing, the Circuits and Systems, the Microwave Theory and Techniques, and the Communications societies, the German Society of Information Technology (ITG), and the Austrian Electrotechnical Association (OVE). He received the dissertation awards from the ITG and the Austrian Society of Information and Communications Technology (GIT) in 2000, the Austrian Kardinal Innitzer award in natural sciences in 2010, and the German ITG award in 2016. From 2009 to 2015, he was member of the editorial board of the International Journal of Electronics and Communications (AEU), and from May 2017 to April 2019 he served as an Associate Editor for the IEEE SIGNAL PROCESSING LETTERS.